Uncertainty Loops in Travel-Time Tomography from Nonlinear Wave Physics

Erica Galetti,* Andrew Curtis, and Giovanni Angelo Meles
School of GeoSciences, The University of Edinburgh, Grant Institute, The King's Buildings, James Hutton Road, Edinburgh EH9 3FE, United Kingdom

Brian Baptie
British Geological Survey, Murchison House, West Mains Road, Edinburgh EH9 3LA, United Kingdom
(Received 7 March 2014; revised manuscript received 20 September 2014; published 6 April 2015)

Estimating image uncertainty is fundamental to guiding the interpretation of geoscientific tomographic maps. We reveal novel uncertainty topologies (loops) which indicate that while the speeds of both low- and high-velocity anomalies may be well constrained, their locations tend to remain uncertain. The effect is widespread: loops dominate around a third of United Kingdom Love wave tomographic uncertainties, changing the nature of interpretation of the observed anomalies. Loops exist due to 2nd and higher order aspects of wave physics; hence, although such structures must exist in many tomographic studies in the physical sciences and medicine, they are unobservable using standard linearized methods. Higher order methods might fruitfully be adopted.

DOI: 10.1103/PhysRevLett.114.148501 PACS numbers: 91.30.Jk, 02.30.Zz, 91.30.Ab

Introduction.—Tomographic imaging of the interior of solid and fluid media has revolutionized science and technology in fields as diverse as medicine [1–3], materials science [4,5], chemistry [6], physics [7,8], biology [9–11], oceanography [12], and geology [13–15]. Practitioners derive insight into medium properties by interpreting tomographically derived images (models); analyzing their uncertainties is key to ensuring that such interpretations are robust [16–19]. A recent paradigm shift in assessing uncertainty is to consider solving for *all* tomographic models that fit recorded data, rather than estimating only a single model or image [17,20,21]. This requires that both algorithmic and parametrization-based constraints on models are reduced to a minimum, as are theoretical simplifications in the physics used to interrogate the medium. In this study we remove most standard simplifications by allowing both model parametrizations and data uncertainties to vary within the inversion, and by removing all linearization of ray propagation physics in Markov chain Monte Carlo tomography (see Supplemental Material [22]). This reveals novel structures that dominate tomographic uncertainty estimates and change interpretations. These structures are shown to derive from the use of variable model parametrization and nonlinear (2nd order and above) physics in ray tracing, and are enhanced when both ray paths and model parametrization vary freely during inversion.

Love-wave tomography of the British Isles.—Within the Earth sciences, tomographic imaging of Earth's crust and uppermost mantle has been revolutionized in recent years by the advent of ambient-noise interferometry [26]. Cross-correlations of pairs of recordings of ambient seismic waves that reverberate within the Earth, produce estimates of band-limited Green's functions between locations of the recording seismometers. Since noise sources are mainly confined to the Earth's near surface, these estimates are usually dominated by surface waves that would have propagated between the two seismometer locations if one had been occupied by a source [27]. The latter is referred to as a *virtual* (imagined) seismic source. Surface-wave travel times between pairs of seismometer locations can thus be measured and used to image the Earth's seismic velocity structure tomographically [28].

We cross-correlated the horizontal components of all pairs of simultaneously recording seismometers across the U.K. in 2001–2003, 2006–2007, and 2010 (years that provided a useful spread of seismometer locations). Virtual sources were thus constructed from each seismometer, providing an estimate of the Love-wave components of interseismometer Green's functions. Seismometer locations and possible interseismometer ray paths are illustrated in Fig. S1 in the Supplemental Material [22], showing a high density of stations and hence rays in the north and southwest, with lower density in the central and eastern U.K. We applied frequency-time analysis to the resulting Green's function estimates to measure the time taken by fundamental-mode Love waves to travel between each pair of seismometers around periods within the main noise band of 6 to 12 s period [29]. Those travel times are then used for travel-time tomography.

We modified the stochastic (reversible-jump Markov chain Monte Carlo—RJMCMC) tomographic method of Bodin and Sambridge [21] to avoid any linearization of the physics of ray propagation. This method allows the Voronoi cell-based model parametrization to vary within the inversion and produces a large family of model

samples, the distribution of which is consistent with the Bayesian posterior probability distribution of the model given the data (travel times) and *a priori* information. The relationship between travel times and velocity is nonlinear in that the travel-time integrand is a nonlinear function of velocity because ray trajectories depend on the velocity structure of the medium itself. Previous studies linearized the physics by fixing the rays at locations consistent with their best estimate of the mean model at successive stages of the tomographic inversion [21]. We trace new rays through every model considered, hence never linearize the overall inverse problem. A large number of model samples (3×10^6 from 16 parallel Markov chains) are generated, out of which 160 000 are selected to be analyzed (details in Supplemental Material [22]).

Figure 1 shows the maps of the mean velocity of 10 s period Love waves (a), and the standard deviation of that velocity at each point across the U.K. (b), both derived from the 160 000 velocity model samples. Consistent with other studies [29,30] and geological expectations, high mean seismic velocities are observed in the metamorphic and igneous complexes of Scotland in the north, Southern Uplands (~55°N), and Cornwall (southwest); low velocities are observed in sediments of the Midland valley (~56°N), Irish Sea (magnified panel), and basins around London in the south.

Off-shore uncertainties are equal to their *a priori* values since few rays visit marine areas. Within the region interrogated by the data, uncertainties are generally lower in the north and southwest of the U.K. where there is a relatively high density of seismometers; uncertainties are higher where the seismometer density is lower. This is also as expected.

The high-uncertainty looplike features such as the one highlighted are not expected. Looking carefully at uncertainty map (b), similar looplike topologies of various shapes and sizes are observed to span much of the U.K. mainland (e.g., around low-velocity anomalies at −3°E50.5°N, −1.5°E51.5°N, −5.5°E51.5°N, and around the high-velocity anomaly at −1°E53°N). Indeed the loops themselves define all of the highest uncertainties observed on land, and conducting synthetic tomography tests across various known velocity structures we find that loops *always* seem to contain the highest uncertainties.

Figure 1(c) shows the uncertainty estimated from the same data using standard linearized (1st order) methods here using fast-marching surface tomography (FMST [31]): ray paths begin at *a priori* estimates of their positions (traced through the prior model, here homogeneous). After iteratively inverting for the best-fit model, retracing rays through that model, and repeating the linearized inversion with rays fixed at their new positions (similar to [29]), uncertainties are estimated from linearized covariances calculated using the final set of rays. No loops are observed, showing that loop structures are not produced when we include only 1st order physics and fix the model parametrization.

In retrospect, similar looplike uncertainty structures are observable in other studies which use transdimensional tomography with fixed ray geometries. These studies

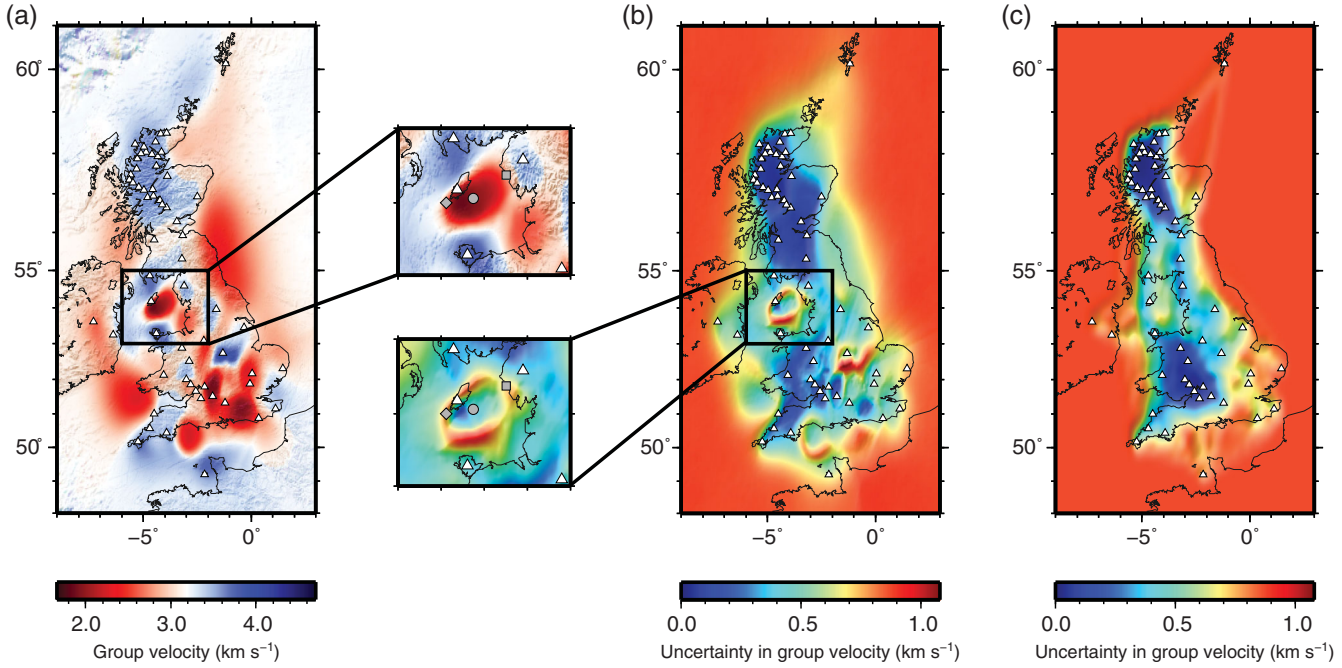

FIG. 1 (color). Ambient-noise Love-wave tomography of the British Isles at 10 s period. (a) Average velocity model; (b) standard deviation map, obtained from an ensemble of 160 000 models, with two details highlighted in magnified plots; (c) standard deviation map for the same data inverted using linearized tomography.

linearize the physics of wave propagation but remain nonlinear in the model parametrization [e.g., Fig. 9(a) of [21]; Fig. 7 of [32]]. To assess the effect of fixed and variable parametrization and ray paths, we performed synthetic tests first using a linearized subspace inversion scheme (FMST [31]), and then using MCMC tomography with either fixed or variable (transdimensional) Voronoi-cell parametrization, and either fixed or variable rays. We found that loops may emerge when either ray paths or model parametrization are allowed to vary freely during inversion (either creates nonlinearity in the model-data relationship). However, when rays are fixed, the uncertainty structure is strictly dictated by the ray geometry regardless of the inversion scheme and type of model parametrization employed, and loops are observed only in extremely fortuitous cases. Also, only a combination of variable ray paths and parametrization were observed to ensure a fully nonlinear estimation of velocity structures and uncertainty without introducing clear ray path- or parametrization-related biases. Tomographic uncertainties are therefore particularly dominated by loop structures only when both parametrization and rays vary freely, explaining why they have not previously been recognized as important features of uncertainty.

Discussion.—To explain the origin of such loops, Fig. 2 shows rays between a single source and receiver through an otherwise homogeneous medium that contains a low velocity anomaly. Although this example simplifies the typical geophysical scenario above, related geometries occur in other fields such as medical tomography and non-destructive testing in materials science.

Since rays are by definition minimum-travel-time paths, Fig. 2(a) illustrates that first-arriving energy does not pass through very low velocity anomalies, but rather refracts around their edges with travel time t_1. This occurs unless the anomaly's velocity becomes sufficiently high that it is equally quick to go around or through the anomaly (third from left plot). The first arriving energy passes through the anomaly if its velocity is higher than this threshold; in that case the travel time is sensitive to the velocity inside the anomaly, and hence changes. Travel-time measurement t_1 therefore only provides an upper bound on velocities of anomalies of fixed shape and size.

Row (b) shows similar phenomena when varying both the anomaly's size and velocity simultaneously. Travel time t_1 is obtained for a larger anomaly with higher velocity (left), or a smaller anomaly with lower velocity (center plots), in each case resulting from energy passing through the anomaly. This occurs down to the same size and velocity threshold as in the top row (third from left plot), beyond which the earliest arriving energy refracts around the anomaly's edge.

The first two plots in row (c) of Fig. 2 show the effect of a variation in the shape of the circular anomaly at which the ray-path switch takes place (third plot). Although the three

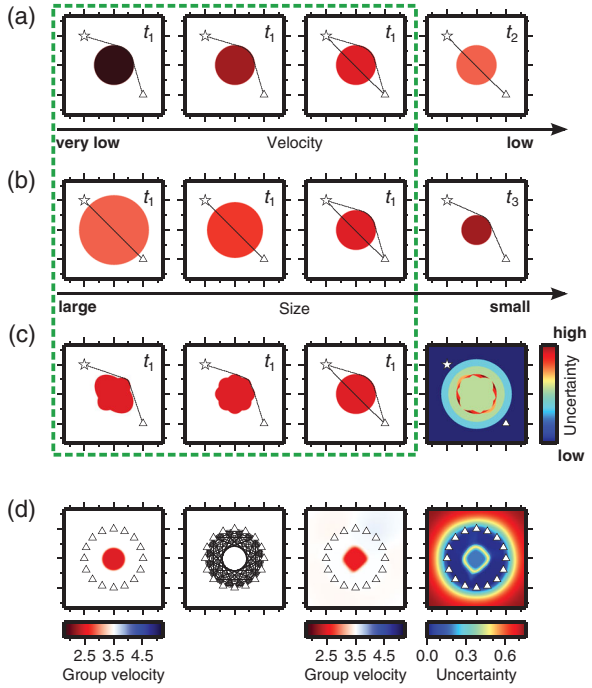

FIG. 2 (color). The effect of a low velocity anomaly (dark to light red) on synthetic rays and travel times. (a) The velocity of the circular anomaly increases from left to right. (b) Both size and velocity of the anomaly decrease from left to right. (c) Three anomalies with similar velocity and size but different shape. The green dashed box encloses velocity models that are all compatible with a given travel time t_1; models on the right produce different travel times t_2 and t_3. The standard deviation across all models within the box is shown in the fourth plot of row (c). (d) Synthetic tomography of the low-velocity anomaly located at the center of an array of receivers: true velocity field and ray paths are shown in the first two plots; ensemble average and uncertainty map from fully nonlinear RJMCMC tomography are in the right two plots.

anomalies have different shapes, the ray path is similar and the same travel time t_1 is obtained. Shapes of all other circular anomalies within the dashed box can vary similarly without affecting the travel time. The fourth plot in (c) shows the uncertainty map obtained by calculating the standard deviation across all models within the dashed box. The largest uncertainties occur in a loop spanning the edges of the anomalies in row (c), resembling the uncertainty loops observed in U.K. tomography.

Now consider the inverse (tomography) problem: all anomalies within the box result in travel time t_1, and for any measured travel time a similar set of plots exist (scaled appropriately). Hence, any travel time only constrains the maximum velocity of a circumnavigable low velocity anomaly (top row of plots), and only constrains the anomaly's boundary to lie within some geometrical bounds (examples in the second and third rows). The anomaly can be further constrained by other sources and receivers, but each individual travel-time measurement results in uncertainty that can be characterized schematically similarly to

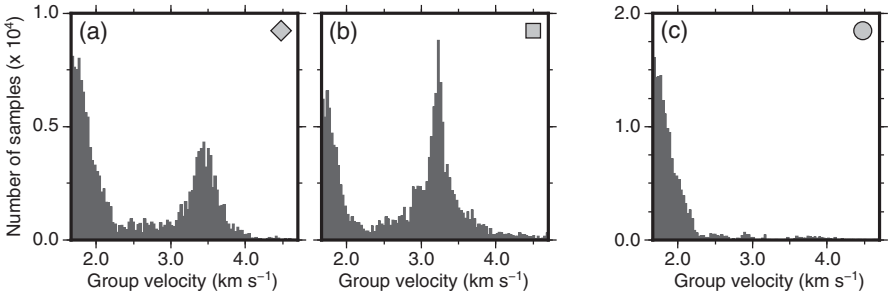

FIG. 3. Posterior probability densities for velocities at different geographical points in the U.K. Histograms are calculated at positions marked by the gray (a) diamond (−4.875°E, 54°N), (b) square (−3.5°E, 54.375°N), (c) circle (−4.25°E, 54.0625°N) in magnified plots in Fig. 1. Points (a) and (b) may be either inside or outside of the anomaly; hence, each has a probability maxima at two velocities and a large range. Point (c) is inside the anomaly and bounded above.

the range of models in Fig. 2. We thus expect an upper-bounded velocity on the interior of low velocity anomalies, and a high velocity uncertainty at any point within some geometrical annulus spanning the edge of each anomaly [the high-uncertainty annulus in the fourth plot of Fig. 2(c)] since that point may lie either inside or outside of the anomaly; hence, its velocity may range from low to high values. The combined effect of both types of uncertainty should thus produce the observed loops of high uncertainty in the locations of anomaly edges, as confirmed by marginal probability histograms in Fig. 3 calculated at three points in Fig. 1.

To check this intuition, row (d) of Fig. 2 shows an application of the fully nonlinear transdimensional algorithm to the synthetic problem above. The first plot in row (d) shows a circular velocity anomaly of velocity 2.5 $\mathrm{km\,s^{-1}}$ within a circular array of receivers and background velocity of 3.5 $\mathrm{km\,s^{-1}}$. To emulate typical ambient-noise tomography scenarios, travel times were calculated along interreceiver paths (true rays are shown in the second plot). The ensemble average and uncertainty map from tomography are shown in the two right plots. The ensemble average approximates the true velocity model and the uncertainty map illustrates that, while the amplitude of the anomaly is reasonably constrained, velocities on its boundaries have far larger uncertainties, producing a looplike structure. Similar experiments showed that loops are thinner and have lower uncertainties around high-velocity anomalies.

In Fig. 1, uncertainty loops appear to exhibit finer spatial detail than the velocity anomalies themselves. Loops define uncertainty in the anomaly boundaries: the loop's thickness therefore depends on the geometry of available seismometer arrays, and generally becomes narrower for denser arrays. Thus uncertainty loops provide a new way to interpret tomographic images: they surround isolated anomalies, and define uncertainty in anomaly shapes. For example, within the magnified Irish Sea, the uncertainty loop shows that the anomaly may extend southeast and be part of another low-velocity anomaly. Also, note that if a discontinuity in the velocity field occurred along a linear boundary, a "line" of high uncertainty (in the location of that boundary) may be observed, rather than a closed loop.

The main difference in character between the models that lie within the dashed box in Fig. 2 and those in the right-hand column is a switch of ray trajectories. Uncertainty loops therefore exist in part because ray paths move. This seems odd since Fermat's theorem states that travel time changes only to second and higher orders with perturbations in ray path caused by velocity changes in the medium. However, that statement concerns the *forward* problem of predicting travel times given a velocity structure. The *inverse* problem consists of attributing observed ray-path-averaged travel times to specific anomalies within the medium. Estimating ray-path geometries is critical to locating these anomalies correctly; hence, such second and higher order effects are central elements of tomography and uncertainty analysis. The latter holds true for both low and high velocity anomalies as both cause ray-path deviations (e.g., the high velocity anomaly at −1°E, 53°N also has a corresponding loop). This explains why uncertainty loops have not been observed to dominate uncertainties previously: they only dominate when both model parametrization and ray paths are allowed to vary freely within the uncertainty analysis, which has almost never been the case in previous (usually linearized) tomography studies.

We thank M. Sambridge and T. Bodin for help with the RJMCMC code, and the Natural Environment Research Council (NERC) and Schlumberger plc for funding this research. Random numbers were generated using the Mersenne Twister routine *genrand* by M. Matsumoto and T. Nishimura (Hiroshima University). Additional help in picking travel times was offered by H. Nicolson and D. Jenkins.

*erica.galetti@ed.ac.uk

[1] B. H. Kevles, *Naked to the bone: Medical imaging in the twentieth century* (Rutgers University Press, New Brunswick, 1996).

[2] G. Wang, H. Y. Yu, and B. De Man, Med. Phys. **35**, 1051 (2008).
[3] G. T. Herman, *Fundamentals of computerized tomography: Image reconstruction from projections*, 2nd ed. (Springer, New York, 2009).
[4] P. Midgley and R. Dunin-Borkowski, Nat. Mater. **8**, 271 (2009).
[5] O. H. Kwon and A. H. Zewail, Science **328**, 1668 (2010).
[6] C. Kim, C. Favazza, and L. H. V. Wang, Chem. Rev. **110**, 2756 (2010).
[7] G. D'Ariano, M. Paris, M. Sacchi, and P. Hawkes, Adv. Imaging Electron Phys. **128**, 205 (2003).
[8] *Quantum state estimation*, edited by M. Paris and J. Řeháček, Lecture Notes in Physics Vol. 649 (Springer, Berlin, Heidelberg, 2004), p. 520.
[9] L. Wang and S. Hu, Science **335**, 1458 (2012).
[10] K. Fridman, A. Mader, M. Zwerger, N. Elia, and O. Medalia, Nat. Rev. Mol. Cell Biol. **13**, 736 (2012).
[11] J. L. S. Milne and S. Subramaniam, Nat. Rev. Microbiol. **7**, 666 (2009).
[12] R. C. Spindel and P. F. Worcester, Sci. Am. **263**, 94 (1990).
[13] G. Nolet, *A breviary of seismic tomography: Imaging the interior of the Earth and Sun* (Cambridge University Press, Cambridge, 2008).
[14] N. Rawlinson, S. Pozgay, and S. Fishwick, Phys. Earth Planet. Inter. **178**, 101 (2010).
[15] T. Tanimoto and T. Lay, Proc. Natl. Acad. Sci. U.S.A. **97**, 12409 (2000).
[16] M. Sambridge, C. Beghein, F. Simons, and R. Snieder, The Leading Edge **25**, 542 (2006).
[17] M. Beaumont and B. Rannala, Nat. Rev. Genet. **5**, 251 (2004).
[18] D. Vasco, L. Johnson, and O. Marques, J. Geophys. Res. [Solid Earth] **108**, 2022 (2003).
[19] W. Y. Song, B. Chiu, G. S. Bauman, M. Lock, G. Rodrigues, R. Ash, C. Lewis, A. Fenster, J. J. Battista, and J. Van Dyk, Int. J. Radiat. Oncol. Biol. Phys. **65**, 595 (2006).
[20] K. Gallagher, K. Charvin, S. Nielsen, M. Sambridge, and J. Stephenson, Mar. Pet. Geol. **26**, 525 (2009).
[21] T. Bodin and M. Sambridge, Geophys. J. Int. **178**, 1411 (2009).
[22] See Supplemental Material at http://link.aps.org/supplemental/10.1103/PhysRevLett.114.148501, which includes Refs. [30–32], for a description of the nonlinear RJMCMC algorithm.
[23] M. Sambridge, N. Rawlinson, in *Seismic earth: Array analysis of broadband seismograms*, Geophysical Monograph Series Vol. 157, edited by A. Levander and G. Nolet (American Geophysical Union, Washington, DC, 2005), p. 49.
[24] T. Bodin, M. Sambridge, N. Rawlinson, and P. Arroucau, Geophys. J. Int. **189**, 1536 (2012).
[25] T. Bodin, M. Salmon, B. L. N. Kennett, and M. Sambridge, J. Geophys. Res. Solid Earth **117**, B10307 (2012).
[26] M. Campillo and A. Paul, Science **299**, 547 (2003).
[27] K. Wapenaar and J. Fokkema, Geophysics **71**, SI33 (2006).
[28] N. M. Shapiro, M. Campillo, L. Stehly, and M. H. Ritzwoller, Science **307**, 1615 (2005).
[29] H. Nicolson, A. Curtis, and B. Baptie, Geophys. J. Int. **198**, 637 (2014).
[30] H. Nicolson, A. Curtis, B. Baptie, and E. Galetti, Proc. Geol. Assoc. **123**, 74 (2012).
[31] N. Rawlinson and M. Sambridge, Explor. Geophys. **36**, 341 (2005).
[32] M. K. Young, H. Tkalčić, T. Bodin, and M. Sambridge, J. Geophys. Res. Solid Earth **118**, 5467 (2013).